Synthesis of multi-wavelength temporal phase-shifting algorithms optimized for high signal-to-noise ratio and high detuning robustness using the frequency transfer function

Manuel Servin,* Moises Padilla, and Guillermo Garnica

Centro de Investigaciones en Optica A. C., Loma del Bosque 115, Col. Lomas del Campestre, 37150 Leon Guanajuato, Mexico

*mservin@cio.mx

Abstract: Synthesis of single-wavelength temporal phase-shifting algorithms (PSA) for interferometry is well-known and firmly based on the frequency transfer function (FTF) paradigm. Here we extend the single-wavelength FTF-theory to dual and multi-wavelength PSA-synthesis when several simultaneous laser-colors are present. The FTF-based synthesis for dual-wavelength (DW) PSA is optimized for high signal-to-noise ratio and minimum number of temporal phase-shifted interferograms. The DW-PSA synthesis herein presented may be used for interferometric contouring of discontinuous industrial objects. Also DW-PSA may be useful for DW shop-testing of deep free-form aspheres. As shown here, using the FTF-based synthesis one may easily find explicit DW-PSA formulae optimized for high signal-to-noise and high detuning robustness. To this date, no general synthesis and analysis for temporal DW-PSAs has been given; only *ad hoc* DW-PSAs formulas have been reported. Consequently, no explicit formulae for their spectra, their signal-to-noise, their detuning and harmonic robustness has been given. Here for the first time a fully general procedure for designing DW-PSAs (or triple-wavelengths PSAs) with desire spectrum, signal-to-noise ratio and detuning robustness is given. We finally generalize DW-PSA to higher number of wavelength temporal PSAs.

OCIS codes: (120.0120) Instrumentation, measurement, and metrology; (120.6650) Surface measurements, figure; (100.2650) Fringe analysis.

References and links

1. M. Servin, J. A. Quiroga, and M. Padilla, *Interferogram Analysis for Optical Metrology, Theoretical Principles and Applications* (Wiley-VCH, 2014).
2. J. C. Wyant, "Testing aspherics using two-wavelength holography," Appl. Opt. **10**(9), 2113–2118 (1971).
3. C. Polhemus, "Two-wavelength interferometry," Appl. Opt. **12**(9), 2071–2074 (1973).
4. Y. Y. Cheng and J. C. Wyant, "Multiple-wavelength phase-shifting interferometry," Appl. Opt. **24**(6), 804–807 (1985).
5. Y. Y. Cheng and J. C. Wyant, "Two-wavelength phase shifting interferometry," Appl. Opt. **23**(24), 4539–4543 (1984).
6. R. Onodera and Y. Ishii, "Two-wavelength interferometry that uses a fourier-transform method," Appl. Opt. **37**(34), 7988–7994 (1998).
7. C. Wagner, W. Osten, and S. Seebacher, "Direct shape measurement by digital wavefront reconstruction and multiwavelength contouring," Opt. Eng. **39**(1), 79–85 (2000).
8. J. Gass, A. Dakoff, and M. K. Kim, "Phase imaging without 2π ambiguity by multiwavelength digital holography," Opt. Lett. **28**(13), 1141–1143 (2003).
9. S. De Nicola, A. Finizio, G. Pierattini, D. Alfieri, S. Grilli, L. Sansone, and P. Ferraro, "Recovering correct phase information in multiwavelength digital holographic microscopy by compensation for chromatic aberrations," Opt. Lett. **30**(20), 2706–2708 (2005).
10. J. Kühn, T. Colomb, F. Montfort, F. Charrière, Y. Emery, E. Cuche, P. Marquet, and C. Depeursinge, "Real-time dual-wavelength digital holographic microscopy with a single hologram acquisition," Opt. Express **15**(12), 7231–7242 (2007).

#260791 Received 8 Mar 2016; revised 15 Apr 2016; accepted 19 Apr 2016; published 26 Apr 2016

11. K. Falaggis, D. P. Towers, and C. E. Towers, "Multiwavelength interferometry: extended range metrology," Opt. Lett. **34**(7), 950–952 (2009).
12. T. Kakue, Y. Moritani, K. Ito, Y. Shimozato, Y. Awatsuji, K. Nishio, S. Ura, T. Kubota, and O. Matoba, "Image quality improvement of parallel four-step phase-shifting digital holography by using the algorithm of parallel two-step phase-shifting digital holography," Opt. Express **18**(9), 9555–9560 (2010).
13. D. G. Abdelsalam, R. Magnusson, and D. Kim, "Single-shot, dual-wavelength digital holography based on polarizing separation," Appl. Opt. **50**(19), 3360–3368 (2011).
14. D. G. Abdelsalam and D. Kim, "Two-wavelength in-line phase-shifting interferometry based on polarizing separation for accurate surface profiling," Appl. Opt. **50**(33), 6153–6161 (2011).
15. U. P. Kumar, N. K. Mohan, and M. Kothiyal, "Red–Green–Blue wavelength interferometry and TV holography for surface metrology," J. Opt. **40**(4), 176–183 (2011).
16. D. Barada, T. Kiire, J. Sugisaka, S. Kawata, and T. Yatagai, "Simultaneous two-wavelength Doppler phase-shifting digital holography," Appl. Opt. **50**(34), H237–H244 (2011).
17. R. Kulkarni and P. Rastogi, "Multiple phase estimation in digital holographic interferometry using product cubic phase function," Opt. Lasers Eng. **51**(10), 1168–1172 (2013).
18. W. Zhang, X. Lu, L. Fei, H. Zhao, H. Wang, and L. Zhong, "Simultaneous phase-shifting dual-wavelength interferometry based on two-step demodulation algorithm," Opt. Lett. **39**(18), 5375–5378 (2014).
19. W. Zhang, X. Lu, C. Luo, L. Zhong, and J. Vargas, "Principal component analysis based simultaneous dual-wavelength phase-shifting interferometry," Opt. Commun. **341**, 276–283 (2015).

1. Introduction

Throughout this paper we assume that the frequency transfer function (FTF) paradigm is known [1]. As far as we know, the first researcher to use dual-wavelength (DW) interferometry was Wyant in 1971 [2]. Wyant used two fixed laser-wavelengths λ_1 and λ_2 to test an optical surface with an equivalent wavelength of $\lambda_{eq} = \lambda_1\lambda_2 / |\lambda_1 - \lambda_2|$ [2]. Thus typically λ_{eq} is much larger than either λ_1 or λ_2 ($\lambda_{eq} >> \{\lambda_1, \lambda_2\}$). Dual-wavelength (DW) interferometry was improved by Polhemus [3], and Cheng and Wyant [4,5] using digital temporal phase-shifting.

On the other hand, Onodera et al. [6] used spatial-carrier double-wavelength digital-holography (DW-DH) and Fourier interferometry for phase-demodulation. This in turn was followed by many multi-wavelength digital-holographic (DH) Fourier phase-demodulation methods in such diverse applications as interferometric contouring [7], phase-imaging [8], chromatic aberration compensation in microscopy [9]; single hologram DW microscopy [10]; comb multi-wavelength laser for extended range optical metrology [11], and a two-steps digital-holography for image quality improvement [12]. DW-DH is already well understood.

Switching back to temporal DW phase-shifting algorithms (DW-PSAs), Abdelsalam et al. [14] have recently reworked this technique. Even though Abdelsalam et al. [14] give working PSA formulas they do not estimate their spectra, their signal-to-noise ratio, or their detuning and harmonics robustness. Kumar et al. [15] and Baranda et al. [16] also provided valid temporal PSA formulas but also failed to characterize their PSAs in terms of signal-to-noise, detuning and harmonic rejection. Another different approach was followed by Kulkarni and Rastogi [17] in which they have demodulated the two interesting phases by fitting a low-order polynomial to each phase. Their approach [17] worked well for the example provided but we think their method could easily cross-talk between fitted polynomials for complicated modulating phases [17]. Yet another approach by Zhang et al. was published [18,19]. Zhang used a simultaneous two-steps [18], and principal component interferometry [19] to solve the dual-wavelength phase-shifting measurement. Zhang et al. used 32 randomly phase-shifted interferograms [19]. Even though Zhang [19] could demodulate the two phases, they used 32 phase-shifted temporal interferograms. All these works on temporal DW-PSA [2–5,14–19] have given just specific DW-PSAs without explicit formulae for their spectra, signal-to-noise, detuning and harmonic robustness.

In contrast to previous *ad hoc* temporal DW-PSA formulas [2–5, 14–19], here we give a general theory for synthesizing DW-PSAs mathematically formalizing their spectrum, their signal-to-noise, and their detuning-harmonic robustness; these are the most important characteristics of any PSA.

#260791 Received 8 Mar 2016; revised 15 Apr 2016; accepted 19 Apr 2016; published 26 Apr 2016

2. Spatial-carrier phase-demodulation for Dual-wavelength (DW) interferometry

Dual-wavelength digital-holography (DW-DH) is well understood and widely used [6–10]. As shown in Fig. 1, in DW-DH the two lasers beams are tilted to introduce spatial-carrier fringes [7]. In Fig. 1 both lasers beams are tilted in the x direction, but in general, for a better use of the Fourier space, one may tilt them independently along the x and y directions [11–14].

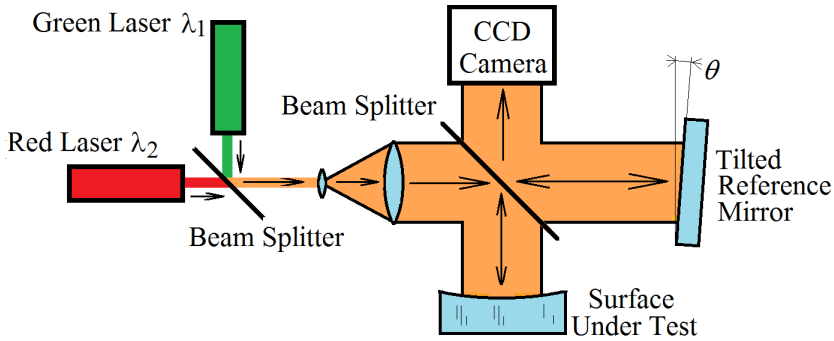

Fig. 1. Schematics for DW-DH using a single tilted reference mirror [6]. The orange-color light-path corresponds to the spatial superposition of the red and green lasers.

The DW-DH obtained at the CCD camera in Fig. 1 may be modeled by,

$$I(x,y) = a(x,y) + b_1(x,y)\cos\left[\varphi_1(x,y) + u_1 x\right] + b_2(x,y)\cos\left[\varphi_2(x,y) + u_2 x\right]. \quad (1)$$

Here $u_1 x = x(2\pi/\lambda_1)\tan(\theta)$ and $u_2 x = x(2\pi/\lambda_2)\tan(\theta)$ are the spatial-carriers of the DW-DH. The reference mirror-angle with respect to the x axis is θ. The searched phases are $\varphi_1(x,y) = (2\pi/\lambda_1)W_1(x,y)$ and $\varphi_2(x,y) = (2\pi/\lambda_2)W_2(x,y)$; being $W_1(x,y)$ and $W_2(x,y)$ the measuring wavefronts. Figure 2 shows a schematic of the Fourier spectrum of Eq. (1).

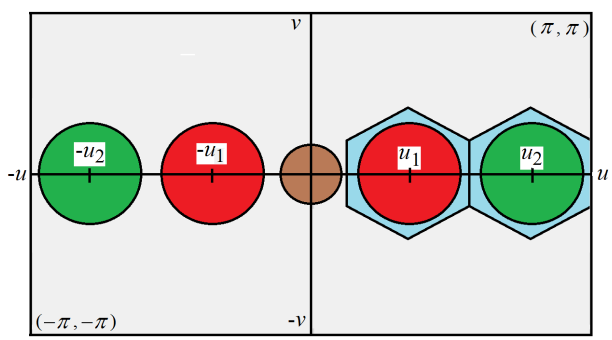

Fig. 2. The hexagons are the spatial quadrature filters which demodulate φ_1 and φ_2.

The two hexagons in Fig. 2 are the spatial quadrature filters that passband the desired analytic signals. After filtering, the inverse Fourier transform find the demodulated phases [1]. The advantage of DW-DH is that only one digital-hologram is needed to obtain $\{\varphi_1, \varphi_2\}$; however its drawback is that just a fraction of the Fourier space $(u,v) \in [-\pi,\pi]\times[-\pi,\pi]$ is used (Fig. 2). This limitation makes DW-DH not suitable for measuring discontinuous industrial objects [7]. In contrast, in DW-PSAs the full Fourier spectrum $(u,v) \in [-\pi,\pi]\times[-\pi,\pi]$ may be used.

#260791 Received 8 Mar 2016; revised 15 Apr 2016; accepted 19 Apr 2016; published 26 Apr 2016

3. Temporal dual-wavelength (DW) phase-shifting interferometry

From now on only temporal interferometry is discussed. The temporal phase-shifting fringes for double-wavelength interferometry may be modeled as,

$$I(x,y,t)=a(x,y)+b_1(x,y)\cos\left[\varphi_1(x,y)+\left(\frac{2\pi}{\lambda_1}d\right)t\right]+b_2(x,y)\cos\left[\varphi_2(x,y)+\left(\frac{2\pi}{\lambda_2}d\right)t\right]. \quad (2)$$

Here $t\in(-\infty,\infty)$, and $\varphi_1(x,y)=(2\pi/\lambda_1)W_1(x,y)$, $\varphi_2(x,y)=(2\pi/\lambda_2)W_2(x,y)$ are the measuring phases. The parameter d is the PZT-step. The fringes background is $a(x,y)$ and their contrasts are $b_1(x,y)$ and $b_2(x,y)$. Figure 3 shows one possible set-up for a DW temporal phase-shifting interferometer.

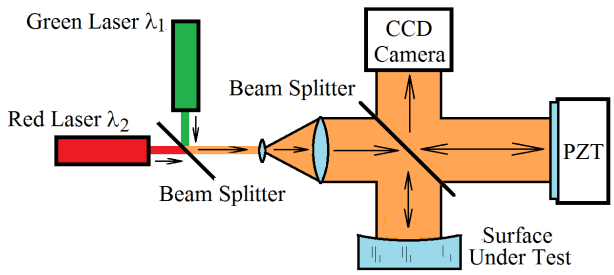

Fig. 3. A schematic example of a temporal-carrier DW interferometer [2–5] for surface measured with equivalent wavelength λ_{eq}; the piezoelectric transducer is PZT.

With 2-wavelengths measurements one can synthesize an equivalent wavelength λ_{eq} [2–19],

$$\lambda_{eq}=\frac{\lambda_1\,\lambda_2}{|\lambda_1-\lambda_2|}\,; \qquad \lambda_{eq}>>(\lambda_1\ or\ \lambda_2)\,. \quad (3)$$

With large λ_{eq} one may measure deeper surface discontinuities or topographies than using either λ_1 or λ_2 [2–19]. For a given PZT-step d, the two angular-frequencies (in radians per interferogram) are given by,

$$\omega_1=\frac{2\pi}{\lambda_1}d, \quad \text{and} \quad \omega_2=\frac{2\pi}{\lambda_2}d. \quad (4)$$

Using this equation one may rewrite Eq. (2) as,

$$I(x,y,t)=a(x,y)+b_1(x,y)\cos\left[\varphi_1(x,y)+\omega_1 t\right]+b_2(x,y)\cos\left[\varphi_2(x,y)+\omega_2 t\right], \quad (5)$$

Here we have 5 unknowns, namely $\{a,b_1,b_2,\varphi_1,\varphi_2\}$. Therefore we need at least 5 phase-shifted interferograms (5-equations) to obtain a solution for $\{\varphi_1,\varphi_2\}$; these are,

$$\begin{aligned}
I_0(x,y)&=a+b_1\cos[\varphi_1]+b_2\cos[\varphi_2],\\
I_1(x,y)&=a+b_1\cos[\varphi_1+\omega_1]+b_2\cos[\varphi_2+\omega_2],\\
I_2(x,y)&=a+b_1\cos[\varphi_1+2\omega_1]+b_2\cos[\varphi_2+2\omega_2],\\
I_3(x,y)&=a+b_1\cos[\varphi_1+3\omega_1]+b_2\cos[\varphi_2+3\omega_2],\\
I_4(x,y)&=a+b_1\cos[\varphi_1+4\omega_1]+b_2\cos[\varphi_2+4\omega_2].
\end{aligned} \quad (6)$$

#260791 Received 8 Mar 2016; revised 15 Apr 2016; accepted 19 Apr 2016; published 26 Apr 2016

For clarity, most (x, y) coordinates were omitted.

4. Fourier-spectrum for temporal DW-PSAs

The Fourier transform of the temporal interferogram (with $t \in (-\infty, \infty)$) in Eq. (5) is:

$$I(\omega) = a\,\delta(\omega) + \frac{b_1}{2}\left[e^{i\varphi_1}\delta(\omega-\omega_1) + e^{-i\varphi_1}\delta(\omega+\omega_1)\right] + \frac{b_2}{2}\left[e^{i\varphi_2}\delta(\omega-\omega_2) + e^{-i\varphi_2}\delta(\omega+\omega_2)\right]. \quad (7)$$

All (x, y) were omitted. As mentioned, $\omega_1 = (2\pi/\lambda_1)d$ and $\omega_2 = (2\pi/\lambda_2)d$ are the two temporal-carrier frequencies in radians/interferogram; Fig. 4 shows this spectrum.

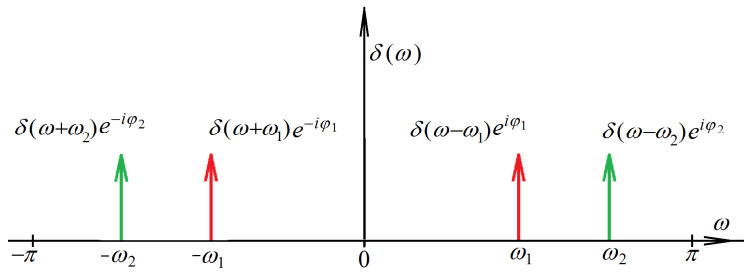

Fig. 4. Fourier spectrum of the DW temporal-carrier interferograms.

Figure 5 shows two ideal frequency transfer functions (FTF), $H_1(\omega)$ and $H_2(\omega)$, that could passband the desired analytic signals $\delta(\omega-\omega_1)\exp(i\,\varphi_1)$ and $\delta(\omega-\omega_2)\exp(i\,\varphi_2)$. Note how each filter is able to passband the desired signals from the same N temporal interferograms.

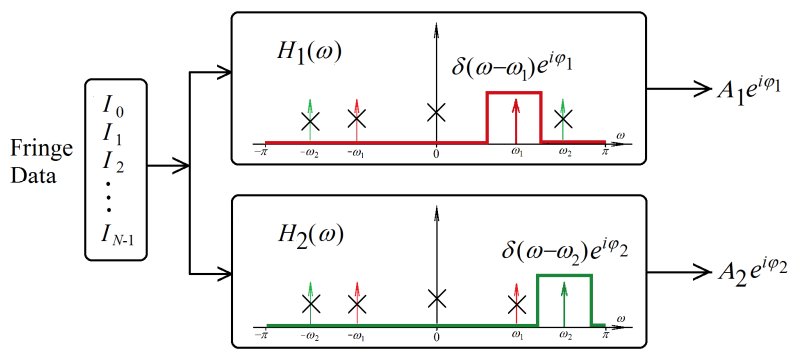

Fig. 5. Ideal spectra of two filters that passband the desired signals $\exp(i\,\varphi_1)$ and $\exp(i\,\varphi_2)$ from N temporal phase-shifted interferograms; all crossed Dirac deltas are filtered-out.

5. Synthesis of DW-PSAs using the FTF and 5-step temporal interferograms

As we know from the FTF-based PSA theory, the rectangular filters in Fig. 5 require a large number N of temporal interferograms [1]. However we can synthesize 5-step bandpass quadrature filters by allocating just 4 spectral-zeroes at frequencies $\{-\omega_2, -\omega_1, 0, \omega_2\}$ for the FTF $H_1(\omega)$, and 4-zeroes at $\{-\omega_2, -\omega_1, 0, \omega_1\}$ for the FTF $H_2(\omega)$ as,

$$\begin{aligned} H_1(\omega) &= \left(1-e^{i\,\omega}\right)\left[1-e^{i(\omega+\omega_2)}\right]\left[1-e^{i(\omega-\omega_2)}\right]\left[1-e^{i(\omega+\omega_1)}\right], \\ H_2(\omega) &= \left(1-e^{i\,\omega}\right)\left[1-e^{i(\omega-\omega_1)}\right]\left[1-e^{i(\omega+\omega_1)}\right]\left[1-e^{i(\omega+\omega_2)}\right]. \end{aligned} \quad (8)$$

#260791 Received 8 Mar 2016; revised 15 Apr 2016; accepted 19 Apr 2016; published 26 Apr 2016

From Eqs. (7)-(8) one sees that $I(\omega)H_1(\omega)$ passband the signal $\exp(i\varphi_1)\delta(\omega-\omega_1)$, while $I(\omega)H_2(\omega)$ bandpass $\exp(i\varphi_2)\delta(\omega-\omega_2)$. Their impulse responses $h_1(t)$ and $h_2(t)$ are,

$$\begin{aligned} h_1(t) &= F^{-1}\{H_1(\omega)\} = \sum_{n=0}^{4} c_{1,n}(\omega_1,\omega_2)\ \delta(t-n), \\ h_2(t) &= F^{-1}\{H_2(\omega)\} = \sum_{n=0}^{4} c_{2,n}(\omega_1,\omega_2)\ \delta(t-n). \end{aligned} \tag{9}$$

Here $c_{1,n}(\omega_1,\omega_2)$ and $c_{2,n}(\omega_1,\omega_2)$ are the 5 complex-valued coefficients that depend on the frequencies $\{\omega_1,\omega_2\}$. Having $\{h_1(t),h_2(t)\}$ the searched DW-PSAs are,

$$\begin{aligned} \frac{1}{2}H_1(\omega_1)b_1(x,y)e^{i\varphi_1(x,y)} &= \sum_{n=0}^{4} c_{1,n}(\omega_1,\omega_2)\ I_n(x,y), \\ \frac{1}{2}H_2(\omega_2)b_2(x,y)e^{i\varphi_2(x,y)} &= \sum_{n=0}^{4} c_{2,n}(\omega_1,\omega_2)\ I_n(x,y). \end{aligned} \tag{10}$$

Where $I_n(x,y)$ are the 5 interferograms. The explicit 5-step DW-PSA to estimate $\varphi_1(x,y)$ is,

$$\begin{aligned} A_1e^{i\varphi_1} &= -e^{i\omega_2}I_0 + c_{1,1}(\omega_1,\omega_2)\ I_1 - c_{1,2}(\omega_1,\omega_2)\ I_2 + c_{1,3}(\omega_1,\omega_2)\ I_3 - e^{i(\omega_2-\omega_1)}I_4, \\ c_{1,1}(\omega_1,\omega_2) &= 1+e^{i\omega_2}+e^{2i\omega_2}+e^{i(\omega_2-\omega_1)}, \\ c_{1,2}(\omega_1,\omega_2) &= 1+e^{i\omega_2}+e^{2i\omega_2}+e^{i(\omega_2-\omega_1)}+e^{-i\omega_1}+e^{i(2\omega_2-\omega_1)}, \\ c_{1,3}(\omega_1,\omega_2) &= \left[1+e^{-i\omega_1}+e^{-i(\omega_2+\omega_1)}+e^{i(\omega_2-\omega_1)}\right]e^{i\omega_2}. \end{aligned} \tag{11}$$

With $A_1 = (1/2)H_1(\omega_1)b_1(x,y)$. Conversely the 5-step DW-PSA to estimate $\varphi_2(x,y)$ is:

$$\begin{aligned} A_2e^{i\varphi_2} &= -e^{i\omega_1}I_0 + c_{2,1}(\omega_1,\omega_2)\ I_1 - c_{2,2}(\omega_1,\omega_2)\ I_2 + c_{2,3}(\omega_1,\omega_2)\ I_3 - e^{i(\omega_1-\omega_2)}I_4, \\ c_{2,1}(\omega_1,\omega_2) &= 1+e^{i\omega_1}+e^{2i\omega_1}+e^{i(\omega_1-\omega_2)}, \\ c_{2,2}(\omega_1,\omega_2) &= 1+e^{i\omega_1}+e^{2i\omega_1}+e^{i(\omega_1-\omega_2)}+e^{-i\omega_2}+e^{i(2\omega_1-\omega_2)}, \\ c_{2,3}(\omega_1,\omega_2) &= \left[1+e^{-i\omega_2}+e^{-i(\omega_1+\omega_2)}+e^{i(\omega_1-\omega_2)}\right]e^{i\omega_1}. \end{aligned} \tag{12}$$

Being $A_2 = (1/2)H_2(\omega_2)b_2(x,y)$. This is the basics for synthesizing DW-PSAs grounded on the FTF paradigm [1]. Previous papers on DW-PSAs [2–5,14–19] stop much shorter than this. They just show particular pairs of DW-PSAs [2–5,14–19] that work for just particular carriers, *i.e.* $(\omega_1,\omega_2) = (1.2, 2.9)$. In this section, we offered DW-PSAs (Eqs. (11)-(12)) which work well (find φ_1 and φ_2) for infinitely-many frequency-pairs $(\omega_1,\omega_2)\in(-\pi,\pi)\times(-\pi,\pi)$. Even if the theory of this paper would stop right here, this paper contains a substantial improvement against current *ad hoc* state of the art in DW-PSA [2–5,14–19].

6. Signal-to-noise power-ratio (SNR) for the FTFs $H_1(\omega)$ and $H_2(\omega)$

Here we review the signal-to-noise power-ratio formulas for PSA quadrature filters [1]. The signal-to-noise power-ratios (SNR) for the FTFs $H_1(\omega)$ and $H_2(\omega)$ are given by [1]:

$$\mathrm{SNR}_1 = \frac{\left|H_1(\omega_1)\right|^2}{\frac{1}{2\pi}\int_{-\pi}^{\pi}\left|H_1(\omega)\right|^2 d\omega}, \qquad \mathrm{SNR}_2 = \frac{\left|H_2(\omega_2)\right|^2}{\frac{1}{2\pi}\int_{-\pi}^{\pi}\left|H_2(\omega)\right|^2 d\omega}. \tag{13}$$

#260791 Received 8 Mar 2016; revised 15 Apr 2016; accepted 19 Apr 2016; published 26 Apr 2016

These SNR-formulas give the power of the signals $\left|H_1(\omega_1)\exp(i\varphi_1)\right|^2$ and $\left|H_2(\omega_2)\exp(i\varphi_2)\right|^2$ divided by their total noise-power $(1/2\pi)\int\left|H_1(\omega)\right|^2 d\omega$ and $(1/2\pi)\int\left|H_2(\omega)\right|^2 d\omega$.

7. Non-optimized DW FTF-based design for $\lambda_1 = 632.8\,\text{nm}$ and $\lambda_2 = 532.0\,\text{nm}$

Let us assume that we use a typical temporal frequency of $\omega_1 = 2\pi/5$ radians per sample for the algorithm $H_1(\omega_1)e^{i\varphi_1(x,y)}$. Having made this choice for ω_1, the frequency ω_2 is set to

$$d = \omega_1\left(\frac{\lambda_1}{2\pi}\right) = \omega_2\left(\frac{\lambda_2}{2\pi}\right) \quad \Rightarrow \quad \omega_2 = \omega_1\left(\frac{\lambda_1}{\lambda_2}\right) \quad \therefore \quad \omega_2 = 1.49\frac{\text{radians}}{\text{sample}}. \tag{14}$$

Giving a PZT-step of $d = 126.6\,\text{nm}$. The DW-FTFs for the two frequencies $\{\omega_1, \omega_2\}$ are:

$$\begin{aligned} H_1(\omega) &= \left(1-e^{i\,\omega}\right)\left[1-e^{i[\omega+1.49]}\right]\left[1-e^{i[\omega-1.49]}\right]\left[1-e^{i(\omega+1.26)}\right], \\ H_2(\omega) &= \left(1-e^{i\,\omega}\right)\left[1-e^{i(\omega-1.26)}\right]\left[1-e^{i(\omega+1.26)}\right]\left[1-e^{i[\omega+1.49]}\right]. \end{aligned} \tag{15}$$

Figure 6 shows the magnitude plot of these two quadrature filters $\{H_1(\omega), H_2(\omega)\}$.

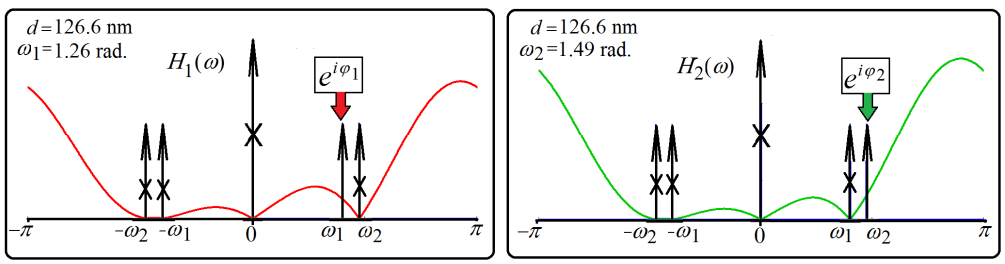

Fig. 6. Spectral plots for the two DW-FTFs $\{H_1(\omega), H_2(\omega)\}$. The crossed Dirac deltas are filter-out signals. These FTFs can demodulate $\{\varphi_1, \varphi_2\}$ with poor signal-to-noise ratio.

The signal-to-noise [1] for the signals $H_1(\omega_1)\exp(i\varphi_1)$ and $H_2(\omega_2)\exp(i\varphi_2)$ are:

$$\frac{\left|H_1(\omega_1)\right|^2}{\frac{1}{2\pi}\int_{-\pi}^{\pi}\left|H_1(\omega)\right|^2 d\omega} = 0.94\,; \quad \frac{\left|H_2(\omega_2)\right|^2}{\frac{1}{2\pi}\int_{-\pi}^{\pi}\left|H_2(\omega)\right|^2 d\omega} = 1.04\,; \quad \omega_1 = 1.26;\, \omega_2 = 1.49. \tag{16}$$

For comparison, a 5-step least-squares PSA has a signal-to-noise power-ratio of 5 [1]. Thus $\omega_1 = 2\pi/5$ and $\omega_2 = 1.49$ were a bad choice. Even though we can estimate $\{\varphi_1, \varphi_2\}$ without cross-talking, from Eqs. (11)-(12), they are going to have poor SNR. Previous efforts in DW-PSAs [2–5,14–19] only provided numeric-specific formulas to obtain $\{\varphi_1, \varphi_2\}$. However, they were absolutely silent about their Fourier spectra, their cross-talk, their signal-to-noise, their harmonics and detuning robustness. All this useful and practical formulae are given here for the first time in terms of the FTFs $\{H_1(\omega_1), H_2(\omega_2)\}$ for designing DW-PSAs. Moreover, in contrast to previous art in DW-PSAs, Eq. (11) and Eq. (12) give infinitely many DW-PSA formulas for continuous pairs of temporal frequencies $(\omega_1, \omega_2) \in (-\pi, \pi)\times(-\pi, \pi)$.

#260791 Received 8 Mar 2016; revised 15 Apr 2016; accepted 19 Apr 2016; published 26 Apr 2016

8. Synthesis of DW-PSAs optimized for signal-to-noise ratio

To find a better selection for $\omega_1 = (2\pi/\lambda_1)d$ and $\omega_2 = (2\pi/\lambda_2)d$, we construct a joint product signal-to-noise ratio as,

$$G_{\mathrm{SNR}}(d) = \left(\frac{|H_1(\omega_1)|^2}{\frac{1}{2\pi}\int_{-\pi}^{\pi} |H_1(\omega)|^2 \, d\omega} \right) \left(\frac{|H_2(\omega_2)|^2}{\frac{1}{2\pi}\int_{-\pi}^{\pi} |H_2(\omega)|^2 \, d\omega} \right); \quad d \in [0, \lambda_{eq}]. \qquad (17)$$

$G_{\mathrm{SNR}}(d)$ has many local maxima, but fortunately it is one-dimensional. Then plot $G_{\mathrm{SNR}}(d)$, look for a good maximum and take the PZT-step *d*. This PZT-step *d* is used to find $\{\omega_1, \omega_2\}$, and the two specific DW-PSA (Eqs. (11)-(12)) which solves the DW interferometric problem.

9. Example of SNR-optimized synthesis for $\lambda_1 = 632.8\,\mathrm{nm}$ and $\lambda_2 = 532\,\mathrm{nm}$

The graph for the signal-to-noise power-ratio product $G_{\mathrm{SNR}}(d)$ with $\omega_1 = (2\pi/\lambda_1)d$, $\omega_2 = (2\pi/\lambda_2)d$ and $d \in [0, \lambda_{eq}]$ is shown next (Fig. 7).

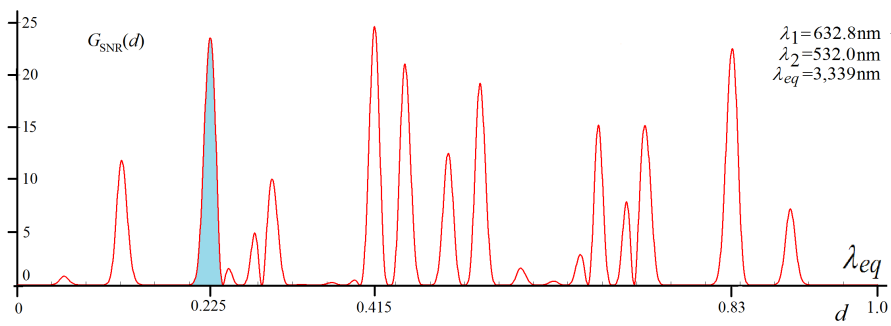

Fig. 7. Graph of $G_{\mathrm{SNR}}(d)$. We kept the third (blue) local maximum at $d = 0.225\lambda_{eq} = 751\,\mathrm{nm}$, for which $G_{\mathrm{SNR}}(d) = 23.5$. Each DW-PSA thus have a signal-to-noise of $\sqrt{23.5} \approx 4.84$.

The first good local maximum is $G_{\mathrm{SNR}}(0.225\lambda_{eq}) \approx 23.5$ (in blue), being $d = 0.225\lambda_{eq}$ or $d = 751\,\mathrm{nm}$. Note that most of this graph is less than 20; *i.e.* $G_{\mathrm{SNR}}(d) < 20$. This means that taking a PZT-step within $d \in [0, \lambda_{eq}]$ *at random*, the probability of landing in a very low signal-to-noise point is *very high*. The FTF graphs for $d = 0.225\lambda_{eq}$ are shown in Fig. 8.

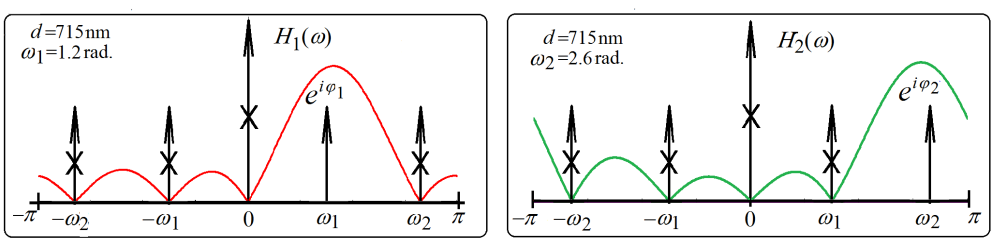

Fig. 8. Spectral plots for the FTFs $H_1(\omega)$ and $H_2(\omega)$ for the SNR-optimized DW-PSA. Note that $\omega_1 = W[(2\pi/\lambda_1)d] = 1.2$ and $\omega_2 = W[(2\pi/\lambda_2)d] = 2.6$; with $W(x) = \arg[\exp(ix)]$.

#260791 Received 8 Mar 2016; revised 15 Apr 2016; accepted 19 Apr 2016; published 26 Apr 2016

Here we have shown that there is a high probability of having a low SNR for the demodulated phases $\varphi_1(x,y)$ and $\varphi_2(x,y)$ without optimizing for $G_{\mathrm{SNR}}(d)$ (Eq. (17)).

10. Example for DW-PSA phase-demodulation for $\lambda_1 = 632.8\,\mathrm{nm}$ and $\lambda_2 = 532.0\,\mathrm{nm}$

Figure 9 shows five computer-simulated interferograms to test the DW-PSAs found in previous section. The PZT-step is $d = 751\,\mathrm{nm}$, giving a good signal-to-noise ratio. As mentioned, for large PZT-steps, the angular frequencies (ω_1, ω_2) are wrapped and given by,

$$\omega_1 = \arg\left[\exp\left(i\,d\,2\pi/\lambda_1\right)\right] = 1.2, \quad \omega_2 = \arg\left[\exp\left(i\,d\,2\pi/\lambda_2\right)\right] = 2.6\,. \qquad (18)$$

Using these angular frequencies in Eq. (11), the specific formula to estimate $\varphi_1(x,y)$ is,

$$A_1(\omega_1)e^{i\varphi_1} = -e^{2.6i}I_0 + (0.78+0.62i)I_1 - (0.5-i)I_2 - (1+0.19i)I_3 - e^{-1.4i}I_4 \qquad (19)$$

Also, from Eq. (12), the specific 5-step DW-PSA to estimate the signal $\varphi_2(x,y)$ is,

$$A_2(\omega_2)e^{i\varphi_2} = -e^{1.2i}I_0 + (0.8+0.6i)I_1 - (0.92-0.1i)I_2 + (0.65-0.77i)I_3 - e^{1.4i}I_4\,. \qquad (20)$$

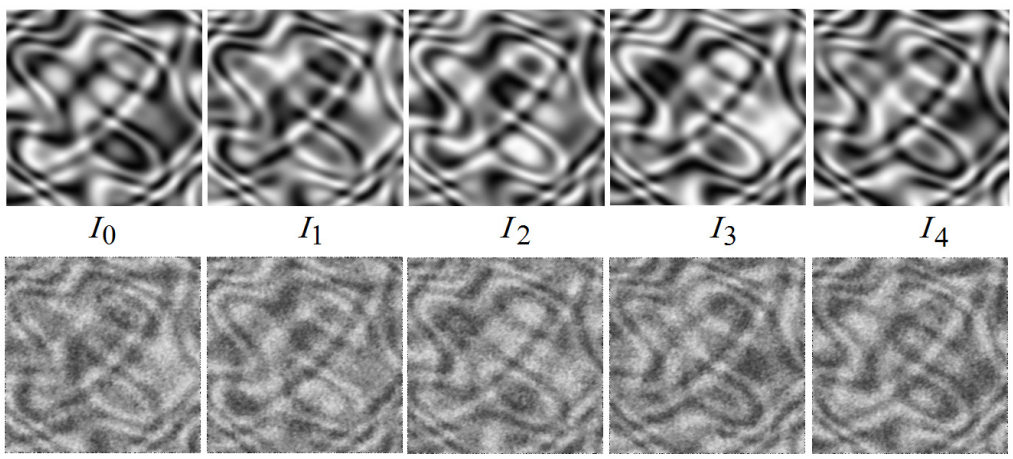

Fig. 9. The upper row shows 5 simulated overlapped interferograms without noise. The lower panel shows the same interferograms corrupted with phase-noise uniformly distributed in [0,π]. The noisy fringes were low-pass filtered by a 3x3 averaging window.

Figure 10 shows the demodulated signals $\varphi_1(x,y)$ and $\varphi_2(x,y)$.

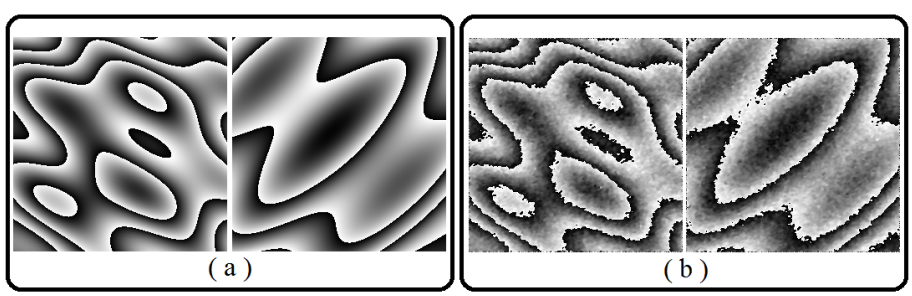

Fig. 10. The demodulated phases $\varphi_1(x,y)$ and $\varphi_2(x,y)$ corresponding to the noiseless (panel (a)) and noisy (panel (b)) 5-steps interferograms in Fig. 9. Please note that there is *absolutely* no cross-talking between the two demodulated phases $\varphi_1(x,y)$ and $\varphi_2(x,y)$.

#260791 Received 8 Mar 2016; revised 15 Apr 2016; accepted 19 Apr 2016; published 26 Apr 2016

Figure 10(a) shows the noiseless demodulated phases, while Fig. 10(b) shows the demodulated phases degraded with a phase noise uniformly distributed within $[0,\pi]$. Note that absolutely no cross-talking between the demodulated phases $\varphi_1(x,y)$ and $\varphi_2(x,y)$ appears.

11. Detuning-robust and SNR-optimized DW-PSA synthesis

Let us assume that our PZT is poorly calibrated. Thus instead of having well-tuned frequencies at $\{\omega_1,\omega_2\}$ we have detuned frequencies at $\{\omega_1+\Delta,\omega_2+\Delta\}$, being Δ the amount of detuning. As Fig. 11 shows, the estimated (erroneous) phase $\hat{\varphi}_2(x,y)$ is now given by,

$$A_2 e^{-i\hat{\varphi}_2} = H_2(-\omega_1-\Delta)e^{-i\varphi_1} + H_2(-\omega_2-\Delta)e^{-i\varphi_2} + H_2(\omega_1+\Delta)e^{i\varphi_1} + H_2(\omega_2+\Delta)e^{i\varphi_2}. \quad (21)$$

The estimated phase $\hat{\varphi}_2(x,y)$ thus have cross-talking from the signals $\{e^{-i\varphi_1}, e^{i\varphi_1}, e^{-i\varphi_2}\}$; conversely $\hat{\varphi}_1(x,y)$ will have distorting cross-talking from $\{e^{-i\varphi_2}, e^{i\varphi_2}, e^{-i\varphi_1}\}$.

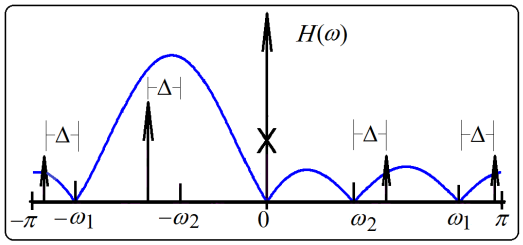

Fig. 11. The effect of detuning (Δ) greatly exaggerated for clarity. The amount of detuning is Δ (radians/sample). The well-tuned frequencies are $\{-\omega_1,-\omega_2,\ \omega_1,\omega_2\}$, while the detuned frequencies are $\{(-\omega_1-\Delta),(-\omega_2-\Delta),(\omega_1+\Delta),(\omega_2+\Delta)\}$.

To have good detuning robustness we need double-zeroes at the rejected frequencies. Therefore, we transform the FTFs in Eq. (8) (5-steps) to detuning-robust FTFs (8-steps) as,

$$\begin{aligned} H_1(\omega) &= \left(1-e^{i\omega}\right)\left[1-e^{i(\omega+\omega_2)}\right]^2\left[1-e^{i(\omega-\omega_2)}\right]^2\left[1-e^{i(\omega+\omega_1)}\right]^2, \\ H_2(\omega) &= \left(1-e^{i\omega}\right)\left[1-e^{i(\omega-\omega_1)}\right]^2\left[1-e^{i(\omega+\omega_1)}\right]^2\left[1-e^{i(\omega+\omega_2)}\right]^2. \end{aligned} \quad (22)$$

Proceeding as before, we need to plot $G_{\mathrm{SNR}}(d)$ and look for a local signal-to-noise maximum. This is shown in Fig. 12 for $\lambda_1 = 632.8\mathrm{nm}$ and $\lambda_2 = 458\mathrm{nm}$.

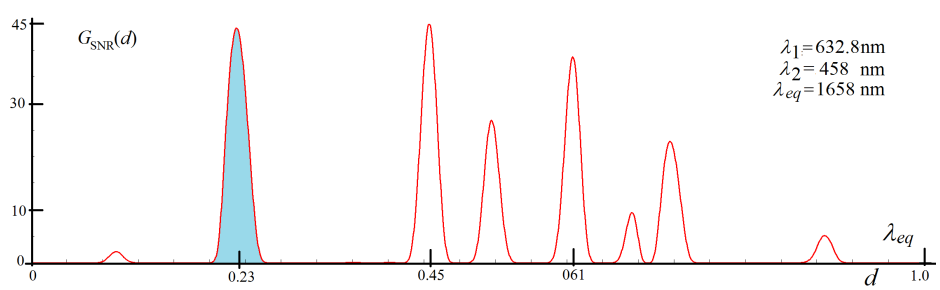

Fig. 12. Joint signal-to-noise product $G_{\mathrm{SNR}}(d)$ of the two detuning-robust FTF-filters $\{H_1(\omega), H_2(\omega)\}$ in Eq. (22). The second maximum has a PZT-displacement of $d = 381\mathrm{nm}$.

#260791 Received 8 Mar 2016; revised 15 Apr 2016; accepted 19 Apr 2016; published 26 Apr 2016

We choose the second maximum (in blue) where $G_{\mathrm{SNR}}\left(0.23\lambda_{eq}\right)=44$, with $d=381\,\mathrm{nm}$. Each 8-step DW-PSA filter in Eq. (22) has a signal-to-noise ratio of about $\sqrt{44}=6.6$. Figure 13 shows the two 8-step detuning-robust FTFs. The spectral second-order zeroes are flatter, so they are frequency detuning Δ tolerant.

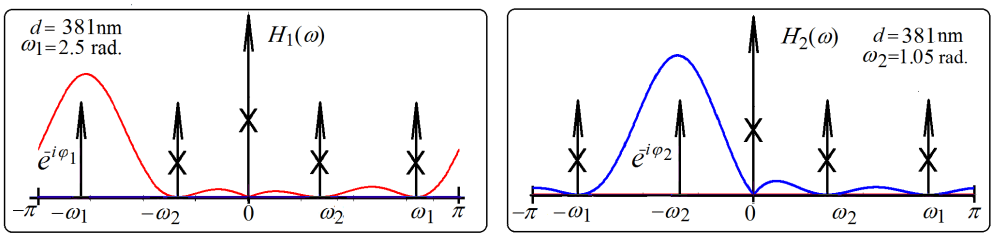

Fig. 13. Spectra of detuning-robust DW-PSA tuned at ω_1=2.5rad and ω_2=1.05rad. The second-order zeroes tolerate a fair amount of frequency detuning Δ.

12. Harmonic rejection for DW-PSAs

The main source of fringe-distorting harmonics is the non-linear response of the CCD-camera used to digitize the interferograms [1]. Therefore instead of having perfect-sinusoidal fringe-profile we may have saturated-distorted fringes containing high harmonic power [1]. Figure 14 shows the harmonic response for the FTFs in Eq. (8). The red-sticks are the fringe harmonics at $(n\omega_1)$, and the green ones are the fringe harmonics at $(n\omega_2)$, $|n|\geq 2$.

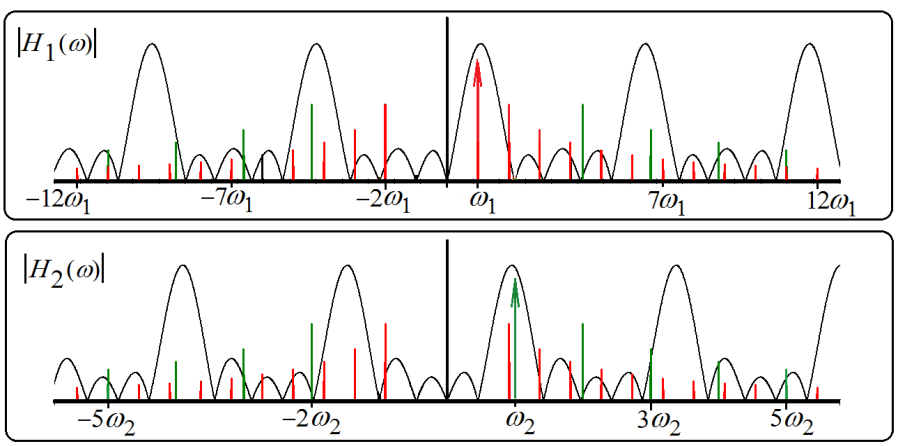

Fig. 14. Harmonic amplitudes for $|H_1(n\omega_1)|$ in red, and $|H_2(n\omega_2)|$ in green. The ideal would be to bandpass just the Dirac-deltas at $\omega=\omega_1$ and $\omega=\omega_2$; but this is not possible.

The power of the desired analytic signals $|H_1(\omega_1)\exp(\varphi_1)|^2$ and $|H_2(\omega_2)\exp(\varphi_2)|^2$ with respect to the sum of their distorting harmonic power is given by,

#260791 Received 8 Mar 2016; revised 15 Apr 2016; accepted 19 Apr 2016; published 26 Apr 2016

$$HR_1 = \frac{\left|H_1(\omega_1)\right|^2}{\sum_{|n|\geq 2}\left\{\left(\frac{1}{n^2}\right)^2\left[\left|H_1(n\,\omega_1)\right|^2 + \left|H_2(n\,\omega_2)\right|^2\right]\right\}} = 11.83,$$

$$HR_2 = \frac{\left|H_2(\omega_2)\right|^2}{\sum_{|n|\geq 2}\left\{\left(\frac{1}{n^2}\right)^2\left[\left|H_1(n\,\omega_1)\right|^2 + \left|H_2(n\,\omega_2)\right|^2\right]\right\}} = 12.2 \tag{23}$$

We assumed that the harmonics amplitude decreases as $(1/n^2)$, so their power decreases as $(1/n^2)^2$. With this assumption the PSA-filters $\{H_1(\omega_1), H_2(\omega_2)\}$ have about 10-times more power than the total power-sum of their harmonics $\{H_1(n\omega_1), H_1(n\omega_2), H_2(n\omega_1), H_2(n\omega_2)\}$.

Figure 15 shows five saturated phase-shifted interferograms. These five temporal interferograms are phase demodulated using DW-PSAs, Eqs. (11)-(12).

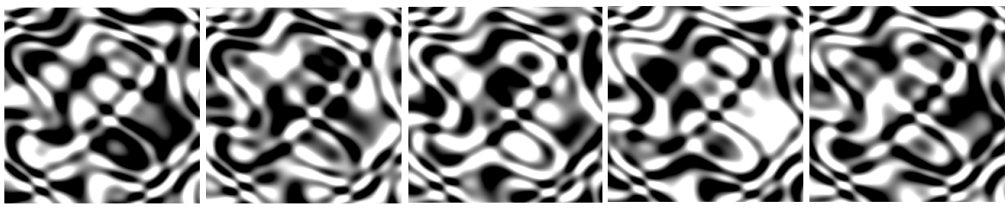

Fig. 15. Five DW phase-shifted temporal interferograms with high amplitude saturation.

Figure 16 shows the distorted demodulated-phases $\{\varphi_1, \varphi_2\}$ of the saturated fringes in Fig. 15.

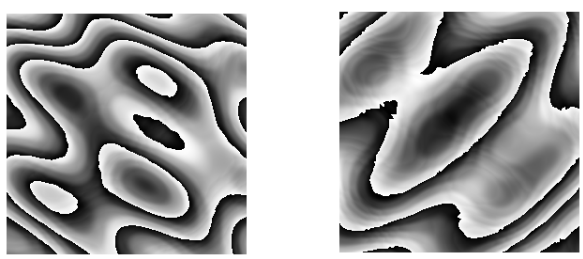

Fig. 16. The demodulated distorted-phases $\{\varphi_1, \varphi_2\}$ from the 5 saturated fringe patterns. Please note that there is a slight harmonics cross-talking between the distorted phases.

13. Multi-wavelength $\{\lambda_1, \lambda_2, ..., \lambda_K\}$ FTF-based phase-shifting algorithms synthesis

Here DW-PSA is generalized to 3-walengths. A simplified schematic of an interferometer simultaneously illuminated with 3-wavelengths $\{\lambda_1, \lambda_2, \lambda_3\}$ is shown in Fig. 17.

#260791 Received 8 Mar 2016; revised 15 Apr 2016; accepted 19 Apr 2016; published 26 Apr 2016

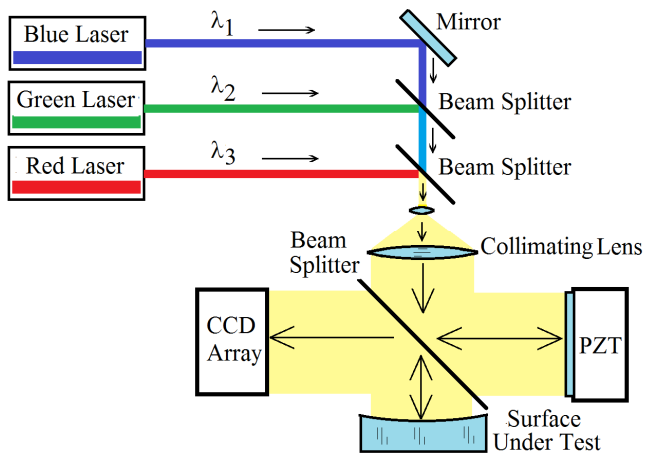

Fig. 17. Simplified schematics for a temporal 3-wavelenght phase-shifting interferometer.

The continuous-time phase-shifted interferogram is,

$$I(x,y,t) = a + b_1 \cos[\varphi_1 + \omega_1 t] + b_2 \cos[\varphi_2 + \omega_2 t] + b_3 \cos[\varphi_3 + \omega_3 t]. \qquad (24)$$

Now Eq. (24) have 7 unknowns $\{a, b_1, b_2, b_3, \varphi_1, \varphi_2, \varphi_3\}$; being $\{\varphi_1, \varphi_2, \varphi_3\}$ the searched phases. Thus we need at least 7 phase-shifted interferograms (7-equations) to find $\{\varphi_1, \varphi_2, \varphi_3\}$. Figure 18 shows the spectrum (for $t \in (-\infty, \infty)$) of this 3-wavelengths temporal-interferograms.

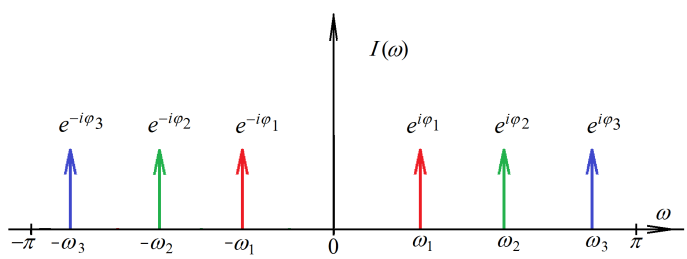

Fig. 18. Fourier spectrum $I(\omega)$ for a 3-wavelength temporal phase-shifted interferograms.

Therefore we need to construct 3-FTFs having at least 6 first-order zeroes (7-steps) as,

$$\begin{aligned}
H_1(\omega) &= \left(1 - e^{i\,\omega}\right)\left[1 - e^{i(\omega+\omega_2)}\right]\left[1 - e^{i(\omega-\omega_2)}\right]\left[1 - e^{i(\omega+\omega_3)}\right]\left[1 - e^{i(\omega-\omega_3)}\right]\left[1 - e^{i(\omega+\omega_1)}\right], \\
H_2(\omega) &= \left(1 - e^{i\,\omega}\right)\left[1 - e^{i(\omega-\omega_1)}\right]\left[1 - e^{i(\omega+\omega_1)}\right]\left[1 - e^{i(\omega+\omega_3)}\right]\left[1 - e^{i(\omega-\omega_3)}\right]\left[1 - e^{i(\omega+\omega_2)}\right], \qquad (25) \\
H_3(\omega) &= \left(1 - e^{i\,\omega}\right)\left[1 - e^{i(\omega-\omega_1)}\right]\left[1 - e^{i(\omega+\omega_1)}\right]\left[1 - e^{i(\omega+\omega_2)}\right]\left[1 - e^{i(\omega-\omega_2)}\right]\left[1 - e^{i(\omega+\omega_3)}\right].
\end{aligned}$$

The FTF $H_1(\omega)$ rejects the analytic signals at $\{-\omega_3, -\omega_2, -\omega_1, 0, \omega_2, \omega_3\}$; the FTF $H_2(\omega)$ rejects the Dirac deltas at $\{-\omega_3, -\omega_2, -\omega_1, 0, \omega_1, \omega_3\}$; and the FTF $H_3(\omega)$ rejects the deltas at $\{-\omega_3, -\omega_2, -\omega_1, 0, \omega_1, \omega_2\}$. Therefore $I(\omega)H_1(\omega)$ isolates $\exp(i\,\varphi_1)\delta(\omega - \omega_1)$; $I(\omega)H_2(\omega)$ isolates $\exp(i\,\varphi_2)\delta(\omega - \omega_2)$, and finally $I(\omega)H_3(\omega)$ obtains $\exp(i\,\varphi_3)\delta(\omega - \omega_3)$.

The joint-product signal-to-noise ratio (SNR) optimizing criterion now reads,

#260791 Received 8 Mar 2016; revised 15 Apr 2016; accepted 19 Apr 2016; published 26 Apr 2016

$$G_{\mathrm{SNR}}(d)=\left(\frac{\left|H_1(\omega_1)\right|^2}{\frac{1}{2\pi}\int_{-\pi}^{\pi}\left|H_1(\omega)\right|^2 d\omega}\right)\left(\frac{\left|H_2(\omega_1)\right|^2}{\frac{1}{2\pi}\int_{-\pi}^{\pi}\left|H_2(\omega)\right|^2 d\omega}\right)\left(\frac{\left|H_3(\omega_3)\right|^2}{\frac{1}{2\pi}\int_{-\pi}^{\pi}\left|H_3(\omega)\right|^2 d\omega}\right). \quad (26)$$

We then find a high local maximum for $G_{\mathrm{SNR}}(d)$, obtaining a fixed PZT-step d, and three angular-frequencies $(\omega_1,\omega_2,\omega_3)\in(-\pi,\pi)\times(-\pi,\pi)\times(-\pi,\pi)$ as,

$$\omega_1=W\left(\frac{2\pi}{\lambda_1}d\right),\quad \omega_2=W\left(\frac{2\pi}{\lambda_2}d\right),\quad \omega_3=W\left(\frac{2\pi}{\lambda_3}d\right);\qquad W(x)=\arg\left[\exp(i\,x)\right]. \quad (27)$$

The three impulse responses $\{h1(t),h2(t),h3(t)\}$ are then given by,

$$\begin{aligned} h_1(t)&=F^{-1}\left\{H_1(\omega)\right\}=\sum_{n=0}^{6}c_{1,n}(\omega_1,\omega_2,\omega_3)\,\delta(t-n),\\ h_2(t)&=F^{-1}\left\{H_2(\omega)\right\}=\sum_{n=0}^{6}c_{2,n}(\omega_1,\omega_2,\omega_3)\,\delta(t-n),\\ h_3(t)&=F^{-1}\left\{H_3(\omega)\right\}=\sum_{n=0}^{6}c_{3,n}(\omega_1,\omega_2,\omega_3)\,\delta(t-n), \end{aligned} \quad (28)$$

Here $c_{1,n}(\omega_1,\omega_2,\omega_3)$, $c_{2,n}(\omega_1,\omega_2,\omega_3)$, $c_{3,n}(\omega_1,\omega_2,\omega_3)$ are the complex coefficients of the PSAs, which now depend on the three temporal-carrier frequencies $\{\omega_1,\omega_2,\omega_3\}$.

We now digitally capture 7 phase-shifted interferograms given by:

$$I_n=a+b_1\cos\left[\varphi_1+n\omega_1\right]+b_2\cos\left[\varphi_2+n\omega_2\right]+b_3\cos\left[\varphi_3+n\omega_3\right];\quad n=0,...,6. \quad (29)$$

With these 7 interferograms we obtain the three searched quadrature analytic signals as,

$$\begin{aligned} A_1\,e^{i\varphi_1(x,y)}&=\sum_{n=0}^{6}c_{1,n}(\omega_1,\omega_2,\omega_3)\;I_n(x,y),\\ A_2\,e^{i\varphi_2(x,y)}&=\sum_{n=0}^{6}c_{2,n}(\omega_1,\omega_2,\omega_3)\,I_n(x,y),\\ A_3\,e^{i\varphi_3(x,y)}&=\sum_{n=0}^{6}c_{3,n}(\omega_1,\omega_2,\omega_3)\;I_n(x,y), \end{aligned} \quad (30)$$

where $A_n=(1/2)H_n(\omega_n)b_n(x,y),\ n=\{1,2,3\}$. By mathematical induction, one may see that a 4-wavelength $\{\lambda_1,\lambda_2,\lambda_3,\lambda_4\}$ phase-shifting algorithm would need at least 9 phase-shifted interferograms, requiring FTFs having 8 first–order zeroes, *et cetera*.

14. Conclusions

The problem that was solved here may be stated as follows: Having a laser interferometer simultaneously illuminated with fixed wavelengths $\{\lambda_1,\lambda_2,...,\lambda_K\}$ and a single PZT phase-shifter, find K phase-shifting algorithms (PSAs) which phase-demodulate $\{\varphi_1,\varphi_2,...,\varphi_K\}$ for each laser-color, with high signal-to-noise and no cross-taking among these phases.

This was solved as follows (for K = 2 sections 3-12, and K = 3 in section 13),

a) First we synthesized two FTF quadrature-filters (Eq. (8)) that bandpass $\exp(i\varphi_1)$ and $\exp(i\varphi_2)$ from 5 phase-shifted interferograms (Eq. (6)) as,

#260791 Received 8 Mar 2016; revised 15 Apr 2016; accepted 19 Apr 2016; published 26 Apr 2016

$$H_1(\omega)=\left(1-e^{i\,\omega}\right)\left[1-e^{i(\omega+\omega_2)}\right]\left[1-e^{i(\omega-\omega_2)}\right]\left[1-e^{i(\omega+\omega_1)}\right],$$
$$H_2(\omega)=\left(1-e^{i\,\omega}\right)\left[1-e^{i(\omega-\omega_1)}\right]\left[1-e^{i(\omega+\omega_1)}\right]\left[1-e^{i(\omega+\omega_2)}\right]. \tag{31}$$

b) We then jointly optimize the FTFs $\{H_1(\omega),H_2(\omega)\}$ for high signal-to-noise $G_{\mathrm{SNR}}(d)$ (Eq. (17)) and obtain the PZT-step d at which that local maximum occurs (Fig. 7).

c) Having an optimum PZT-step d, we then calculated the tuning frequencies $\omega_1=(2\pi/\lambda_1)d$, $\omega_2=(2\pi/\lambda_2)d$, which substituted back into $\{H_1(\omega),H_2(\omega)\}$ gave us the specific DW-PSAs that demodulate $\varphi_1(x,y)$ and $\varphi_2(x,y)$ (Eqs. (11)-(12)).

d) We plotted (Fig. 8) the SNR-optimized FTF designs $\{H_1(\omega),H_2(\omega)\}$ to gauge their spectral behavior within $\omega\in(-\pi,\pi)$. We also plotted (Fig. 14) these optimized FTFs for an extended frequency range $\omega\in[-20\pi,20\pi]$, to gauge their harmonic-rejection.

e) We used the SNR-optimized FTF-designs to phase-demodulate 5 phase-shifted interferograms (Figs. 9–10) with high signal-to-noise and no phase cross-talking.

f) For poor PZT-calibration we modified the FTFs $\{H_1(\omega),H_2(\omega)\}$ by raising the first-order zeroes to second-order ones, *i.e.* $(\omega-\omega_1)\Rightarrow(\omega-\omega_1)^2$, $(\omega-\omega_2)\Rightarrow(\omega-\omega_2)^2$, etc.; making $\{H_1(\omega),H_2(\omega)\}$ robust to detuning at the rejected frequencies (Fig. 13).

g) With the SNR-optimized FTFs $\{H_1(\omega),H_2(\omega)\}$ we quantified the harmonic-rejection capacity for each $\{H_1(\omega),H_2(\omega)\}$ using Eq. (23).

h) Finally in section 13, we extended the DW FTF-based theory to 3-wavelengths $\{\lambda_1,\lambda_2,\lambda_3\}$; further *K*-wavelengths $\{\lambda_1,\lambda_2,...,\lambda_K\}$ generalization of this FTF-based multi-wavelength PSA theory is just a matter of mathematical induction.

As far as we know, previous art on DW-PSAs [2–5,14–19] only provided *ad hoc* multi-wavelength PSA designs. Thus, this is the first time that a general theory for synthesizing and analyzing multi-wavelength temporal phase-shifting algorithms is presented, and from which one may derive quantifying formulas for: (a) the PSAs spectra for each wavelength, (b) the PSAs signal-to-noise robustness for each wavelength, (c) the PSAs detuning sensitivity, and (d) the PSAs harmonics rejection for each wavelength. Finally, we presented two computer simulated examples of 5 DW phase-shifted interferograms with $\lambda_1=632.8\text{nm}$ and $\lambda_2=532\text{nm}$ in order to illustrate the behavior of our synthesized FTF-based DW-PSAs.

Acknowledgments

The authors acknowledge the financial support of the Mexican National Council for Science and Technology (CONACYT), grant 157044. Also the authors acknowledge Cornell University for supporting the e-print repository arXiv.org and the Optical Society of America for permitting OSA's contributors to post their manuscript at arXiv.